Simulations of Spherical and Helical Beam with MATLAB

Undergraduate Project (EP-392 & EP-491) report submitted to

Indian Institute of Technology (BHU) Varanasi

in partial fulfilment for the award of the degree of

Bachelor and Master of Technology

in

Engineering Physics

by

Vedang Kshirsagar

(19174013)

Under the supervision of

Dr. Rakesh Kumar Singh

Department of Physics

Indian Institute of Technology (BHU) Varanasi

Even Semester, 2021-22 & Odd Semester, 2022-23

December 12, 2022

DECLARATION

I certify that

(a) The work contained in this report has been done by me under the guidance of my supervisor.

(b) The work has not been submitted to any other Institute for any degree or diploma.

(c) I have conformed to the norms and guidelines given in the Ethical Code of Conduct of the Institute.

(d) Whenever I have used materials (data, theoretical analysis, figures, and text) from other sources, I have given due credit to them by citing them in the text of the thesis and giving their details in the references. Further, I have taken permission from the copyright owners of the sources, whenever necessary.

Date: December 12, 2022   (Vedang Kshirsagar)

Place: Varanasi   (19174013)

DEPARTMENT OF PHYSICS
INDIAN INSTITUTE OF TECHNOLOGY (BHU) VARANASI

VARANASI - 221005, INDIA

CERTIFICATE

This is to certify that the project report entitled "**Simulations of Spherical and Helical Beam with MATLAB**" submitted by **Vedang Kshirsagar** (Roll No. 19174013) to Indian Institute of Technology (BHU) Varanasi towards partial fulfilment of requirements for the award of degree of Bachelor and Master of Technology in Engineering Physics is a record of bona fide work carried out by him under my supervision and guidance during Even Semester, 2021-22 & Odd Semester, 2022-23.

Date: December 12, 2022

Place: Varanasi

Dr. Rakesh Kumar Singh

Department of Physics

Indian Institute of Technology (BHU)

Varanasi

Varanasi - 221005, India

Abstract

Name of the student: **Vedang Kshirsagar**   Roll No: **19174013**

Degree for which submitted: **Bachelor and Master of Technology**

Department: **Department of Physics**

Thesis title: **Simulations of Spherical and Helical Beam with MATLAB**

Thesis supervisor: **Dr. Rakesh Kumar Singh**

Month and year of thesis submission: **December 12, 2022**

This report summarizes a study focused on understanding a non-interferometric approach to quantitatively determine the topological charge (ℓ) and phase structure of vortex beams when disrupted by random scattering media. The method involves utilizing the correlation of Stokes parameters (SPS) from a randomly distributed field. The study includes both theoretical and experimental analyses conducted in a laboratory setting and with the assistance of MATLAB.

Acknowledgements

Contents

Chapter 1

Vortex Beams

1.1 Introduction

An optical vortex beam is a light wave or a beam that has a phase singularity at
the nucleus of its wavefront structure with a certain topological charge (ℓ), giving
rise to an intensity null condition or a hollow intensity distribution [Shen et al.
(2019)]. Such a beam with helical phase fronts and orbital angular momentum
reveals a subtle connection between macroscopic physical optics and microscopic
quantum optics. These amazing properties provide a new understanding of a wide
range of optical and physical phenomena, including twisting photons, spin–orbital
interactions, Bose–Einstein condensates, etc., while the associated technologies for
manipulating optical vortices have become increasingly tuneable and flexible. As a
typical representative of optical vortices (OVs), a vortex beam (VB) has become a
classical tool to study the properties of OVs because its generation can be easily
realized in the laboratory [Sarkar et al. (2021)].

1.2 Related Works

From [Shen et al. (2019)], in 1989, Coullet et al. found the vortex solutions of the
Maxwell-Bloch equations and created the concept of OVs, inspired by hydrodynamic
vortices. In 1992, Allen et al. proposed the orbital angular momentum (OAM) in

vortex beams (VBs) where the OVs propagate in paraxial beams, which unveiled a new understanding of the connection between macroscopic optics and quantum effects. In 2001, Zeilinger's group realized the OAM-entangled photon pair, bringing OVs or twisted photons into quantum applications. In 2002, Dholakia's group trapped particles with controlled rotation and a three-dimensional structure by VBs, expanding the applications of optical tweezers. In 2003, Harwit demonstrated astrophysical OAM light generation and its applications in astrometry. In 2004, Zhuang used VBs as tweezers to assemble DNA biomolecules, opening biomedical applications of OVs. In 2005, Ritsch-Marte's group used OAM in microscopy and imaging, and Tamburini et al. reported a super-diffraction-limit imaging approach using OAM. In 2008, Barreiro et al. presented a coding technology using OAM, giving VBs a great advantage for use in optical communications. In 2010, the optical lattice in far-field diffraction of OVs was unveiled as a very prompt and handy way to detect TC. In 2011, Capasso's group proposed the generalized laws of reflection and refraction, guiding OV generation in nanoscale meta-surfaces. In 2012, OAM beams were directly generated in a nanoscale emitter. In 2013, Willner's group demonstrated terabit-scale high-capacity optical communication via OAM multiplexing in both free space and fibers. In 2016, Zeilinger's group generated extreme OAM states of over 10,000 $\hbar$ and realized quantum entanglement of these states.

1.3 Origin

The origin of Vortex Beam takes place in the following manner. Consider a monochromatic transversely polarised field with orthogonal axes x and y. One polarisation component has a twisted phase structure, while the other does not, and the two are coaxially propagating along the z-axis [Sarkar et al. (2021)]. The complex field at $z = 0$ in the transverse plane is written as

$$E(\hat{i}) = A_l(\hat{i}) * \exp(\iota * \ell * \phi)\hat{e_x} + A(\hat{i})\hat{e_y} \qquad (1.1)$$

where r is the spatial location vector in the transverse plane and $\hat{e_x}$, and $\hat{e_y}$ are the horizontal and vertical polarisation states of the light, respectively. The amplitude of the vortex beam is $A_l(r)$, while the amplitude of the nonvortex beam is $A(r)$.

The spiral phase structure of the vortex beam with the topological charge (ℓ) is represented by $\exp(\iota * \ell * \phi)$. The coherent beam now travels through a random scattering medium and arrives at an observation plane in any arbitrary plane z.

$$E(r) = FR(E(r) * \exp(\iota * \Delta(r))) \tag{1.2}$$

where $E(r)$ is the scattered field at the observation plane and $\Delta(r)$ is the spatial random phase. FR is the Fresnel transform corresponding to a distance z. Now the coherent beam propagates through a random scattering medium and reaches an observation plane located at any arbitrary plane z. The speckle pattern at any arbitrary z-plane is given as

$$E(r) = FR(E(\hat{r}) \exp(\iota * \delta(\hat{r}))) \tag{1.3}$$

$$\therefore E(r) = E_x(r)\hat{e_x} + E_y(r)\hat{e_y} \tag{1.4}$$

where $E(r)$ denotes the scattered field at the observation plane, $\delta(\hat{r})$ stands for the spatial random phase introduced by a nonbirefringent random scatterer, r is the spatial position vector at the observation plane and FR represents the Fresnel transform corresponding to propagation at a distance z from the source.

1.4 Properties

1.4.1 Reflection and Refraction

The reflection of a VB generally does not satisfy the classical reflection law, i.e., the angle of incidence θ_i. Instead, the reflected light has a spatial deflection effect related to the OAM of the VB. The difference between θ_i and θ_r is related to the OAM of the beam, obeying the generalized law of reflection

$$sin(\theta_r) - sin(\theta_i) = (\lambda/2 * \pi * \eta) * (\partial\phi/\partial x) \tag{1.5}$$

where λ and ϕ are the wavelength and phase of the light beam, respectively, and η is the refractive index of the medium. In addition, the refraction of VBs does not

satisfy Snell's law, i.e., $\eta_t sin(\theta_t) = \eta_i sin(\theta_i)$ The refraction is related not only to the angles of incidence and refraction ($\theta_i \& \theta_t$ and the refractive indices but also to the OAM, obeying the generalized law of refraction

$$\eta_t * sin(\theta_t) - \eta_i * sin(\theta_i) = (\lambda/2 * \pi) * (\partial\phi/\partial x) \tag{1.6}$$

1.4.2   Interference

For a VB, the pattern of equal-inclination interference with a plane wave is not equispaced fringes but fringes with bifurcation at the singularity of the vortex, and the morphology of the bifurcation is related to the OAM of the beam. The equal-thickness interference pattern of a VB with a plane wave is not Newton's rings but spiral stripes extending outward from the vortex singularity, the number of which is related to the OAM. The self-interference pattern can also show some bifurcation fringes. The interferometric method includes the Mach-Zehnder interferometer, lateral shear interferometer, improved multipoint interferometer, and double-slit interference. These special interference fringes can be used in the detection and measurement methods of vortices.

1.4.3   Diffraction

VBs have unique diffraction properties, the aperture diffraction patterns of which are coupled with the actual OAM. Since Hickmann et al. unveiled in 2010 the exotic lattice pattern in triangular-aperture far-field diffraction of VBs, it has been used as an effective method for OAM detection and measurement of femtosecond vortices, non-integer charge vortices, and elliptical VBs. Many other unique far-field diffraction patterns were investigated through a slit, a square aperture, a diamond-shaped aperture, a circular aperture, an off-axis circular aperture, an isosceles right triangular aperture, a sectorial screen, and so on. The Fresnel diffraction of VBs was also studied. Some special VBs, such as vector VBs and SU (2) VBs, can even bring about special lattice structures in diffraction patterns. The diffraction method includes the use of a triangular aperture, an angular aperture, annular gratings,

astigmatism, and a translated single slit. These special diffraction patterns can be used in vortex detection and measurement methods.

1.5 Generation

The vortex generation methods can be divided into passive vortex generators (converting the fundamental Gaussian beams into VBs by using dynamic or geometric phase plates, meta-surfaces, SLMs, etc.) and active vortex laser generators (such as free space or fiber vortex lasers and nano integrated OAM generators). The OAM-tuneable beams include TC-tuneable and multi-singularity-tuneable beams.

1.5.1 Passive Generation

1.5.1.1 Dynamic Phase Plate

The generation of an optical vortex beam upon accumulated propagation effect relies on physical propagation distance, passing through a media with a given refractive index. An SPP is such an element with a gradient of thickness varying along azimuthal angle according to

$$\partial h / \partial \psi = (\ell * \lambda)/2 * \pi * (n-1) \tag{1.7}$$

where η is the refractive index of the material and λ is the free-space wavelength of the beam. When light passes through an SPP, a helicoidal phase is imposed into the wavefront. To minimize the distortion of the wavefront and precisely produce the desired topological charge for a certain wavelength, the surface quality of SPP needs to be well controlled.

1.5.1.2 Geometric Phase Plate

When a polarized beam undergoes a closed loop on the Poincaré sphere, it acquires not only a dynamic phase but also a geometric phase, which is half of the solid angle in the closed loop on the Poincare sphere. The phase velocity of two linearly orthogonal polarized components is different when light is propagating in an anisotropic

material. The natural anisotropic material normally refers to crystals with different optical axes. By applying external fields on any isotropic material that temporally or permanently breaks the symmetry of the dielectric tensors along the propagation direction, for example, applying electric or magnetic fields, or mechanical stress fields, artificial optical anisotropic materials can be created.

1.5.1.3 Hybrid Phase Plate

Phase compensation for full wavefront control

The independent behavior of engineering dynamic and geometric phases provides more freedom for phase modulation using nanostructures. The broadband nature of the geometric phase was used to compensate for the dispersion of the coupling resonances of metallic and dielectric nanostructures, enabling the operation of the device in a broad spectral range. A single or localized resonance is not sufficient for modifying the phase within a full coverage. Except for tunning multiple resonances or the coupling strength between adjacent scatters, modifying the polarization to introduce a Pancharatnam-Berry phase was adopted into designing hybrid meta-surfaces for full wavefront control.

Multifunctional spin-dependent optical vortex beam generation

In some of the applications, the intrinsic high divergence of a vortex beam during propagation may not be preferred. Instead of introducing a bulky element to focus the beam, an ultrathin element directly generates a focusing vortex beam is desired. A complex phase profile $\phi = 2 * \pi * \lambda(f - \sqrt{(\rho^2 + f^2)}) + \ell * \psi * \phi = 2 * \pi * \lambda(f - \sqrt{(\rho^2 + f^2)}) + \ell * \psi$ where f is the focal length. This complex phase profile is required, each component can be modulated by dynamic and geometric phases independently. More complex multifunctional phase structures of a vortex beam also can be created via a hybrid phase plate.

Arbitrary spin-orbital angular momentum conversion

Optical vortex beams carrying orbital angular momentum generated via geometric phase meta-surfaces arising from the spin-orbit interaction by polarization manipulation have been demonstrated. When passing through a geometric phase plate

with 100% polarization conversion efficiency, namely the phase retardation is $\delta = \pi$, the polarization states will be totally converted to its opposite states. Due to the rotational symmetric geometry, the output OAM states are constrained to be conjugated. The transformation process of a pair of orthogonal circularly polarized states passing through a geometric phase plate can be written as a comparison of the spin-orbit interaction via a rotationally symmetric dynamic phase which manifests the transformation process in a similar way, without changing its polarization states $(\ell_1 = \ell_2)$ and achieving a global OAM state.

1.5.2 Active Generation

1.5.2.1 Free space optical vortex lasers

By inserting an SPP into the laser cavity as a black reflector it introduces high losses to all other modes while it is almost lossless for the desired helical mode. Since then, many approaches have been implemented for vortex laser creation using phase-only, amplitude-only, and phase-amplitude combination optical elements. For laser cavities based on amplitude-only optical elements, most of them are not capable of creating the desired helical wavefront, but instead, they simultaneously produce two LG modes of the opposite but equal azimuthal index, resulting in zero net OAM output. This kind of superposition of OAM modes has been demonstrated in many cavities with special elements, such as spot-defect mirrors SLMs, a pair of Porro prisms, an aberrated lens, and an angular light pumping profile.

A recent study shows that the handedness of OAM modes can be controlled by employing a novel mode selection element (MSE) consisting of two thin aluminum stripes, which introduces a higher loss for one helicity. Optical vectorial vortex beams carrying a singularity on its phase front with spatially inhomogeneous polarization states were found to have many potential applications. The OAM lasers discussed above are continuous wave (CW) lasers. However, an optical vortex pulsed laser with Q-switched operation and self-mode-locked Laguerre-Gaussian lasers with tuneable OAM output was also demonstrated.

1.5.2.2   Integrated OAM lasers

Along with recent advances in the field of nanofabrication and engineered optical materials, the integration of devices has become the inevitable trend of modern photonics. There is an increasing demand for the realization of vortex lasing on an integrated chip. Integrated optical vertex lasing can be implemented by adding an integrable vortex generator element at the output port of the light source or generating a vortex beam inside the light source cavities directly. A micro-vortex laser was implemented by employing a micro-SPP on the output port of a vertical cavity surface emitting laser.

1.5.3   Others

All the other methods and techniques of generating a vortex beam fall in this category. This category is very wide and requires an in-depth understanding of the subject in order to understand how some of these techniques generate the vortex beam. As a result, we would not be dealing with this type in this project.

1.6   Applications

Along with the applications in the fields of microscopy and imaging and optical communication, vortex beams are used in the fields of Quantum Entanglement, Nonlinear Optics, Nanotechnology, Optical Machining, Optical Tweezers, Biomedicine and Chemistry, Metrology, and Astronomy. Overall, there are currently numerous promising and amazing applications related to OVs with unlimited possibilities that require further exploration.

1.6.1   Microscopy and Imaging

The unique spiral phase of VBs can be used in phase-contrast microscopy, demonstrating high-resolution micro-imaging. Applying OAM analysis in the imaging method, the novel digital spiral imaging technique was proposed to improve the
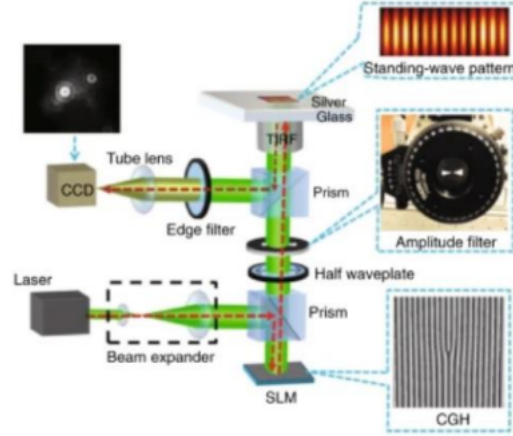
FIGURE 1.1: Applications in microscopy and imaging techniques Shen et al. (2019)

resolution. Currently, imaging using OAM has already realized super-diffraction-limit resolution. In recent years, a growing number of novel microscopy and imaging technologies using VBs have emerged, reaching increasingly higher resolution. For instance, plasmonic structured illumination microscopy using standing surface plasmon waves induced by OVs was proposed, realizing high-resolution wide-field imaging. This microscopy was further improved by using perfect VBs (VBs with a controllable ring radius) to enhance the excitation efficiency and reduce the background noise. With the development of multi-singularity beams, a vortex array was used to harness the point spread function to realize high-resolution far-field microscopy. Specifically, fractional VBs were also used for precise microscopy to reach sub-100-nm resolution. With the advanced vector VBs having a special polarization structure, the super-resolution imaging reached an even higher resolution. With the quantum properties of VBs, quantum ghost imaging was combined with twisted photons, opening new routes for imaging techniques.

1.6.2 Optical Communication

In addition to the polarization, amplitude, pulse shape, and wavelength of light, the OAM can be used as an alternative degree of freedom for multiplexing modulation, enlarging the capacity of optical communication, which is also referred to as
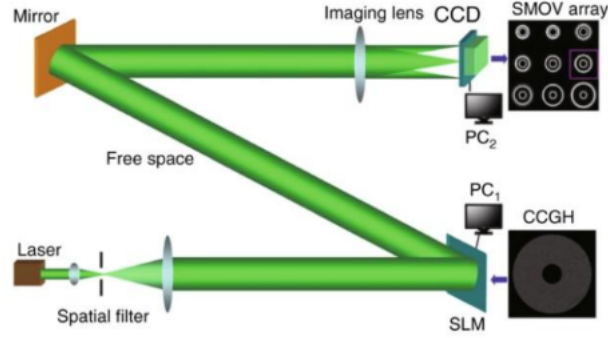
FIGURE 1.2: Schematic of sidelobe-modulated OVs for free-space communication
Shen et al. (2019)

mode/spatial-division multiplexing (MDM/SDM). Optical communication by OAM multiplexing has enabled breaking the Tbit level, much beyond the conventional scheme, thus greatly broadening the application scope. With the study of VB propagation in the atmosphere, free-space communication using vortices was gradually improved. Furthermore, a sidelobe-modulated OV method was proposed for free-space communication with a significant increase in the data transmission capacity. With the development of multi-singularity-tuneable VBs, the capacity and speed of communication can be further improved. A variety of special fibers for OAM mode transmission were designed to enable fiber-based vortex communication technology. Recently, a new OAM multiplexing technology using Dammann vortex gratings in fiber-free-space coupled systems realized massive OAM state parallel detection, offering an opportunity to raise the communication capacity to the Pbit level. OAM-multiplexing- based communication was also demonstrated under many extreme circumstances, such as underwater communication, high-dimensional quantum communication, and long-distance fiber communication.
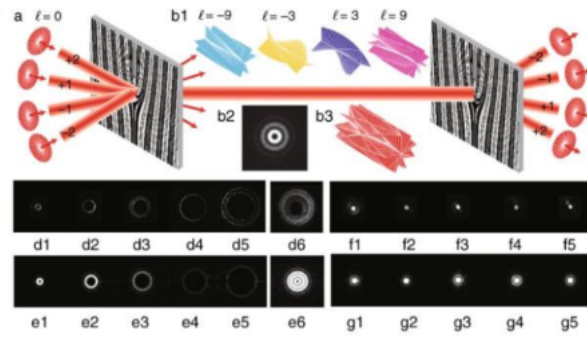
FIGURE 1.3: Dammann-grating-enabled OAM multiplexing technology raising the large capacity to the Pbit level Shen et al. (2019)

Chapter 2

Recovery of Vortex Beam through Scattering Media
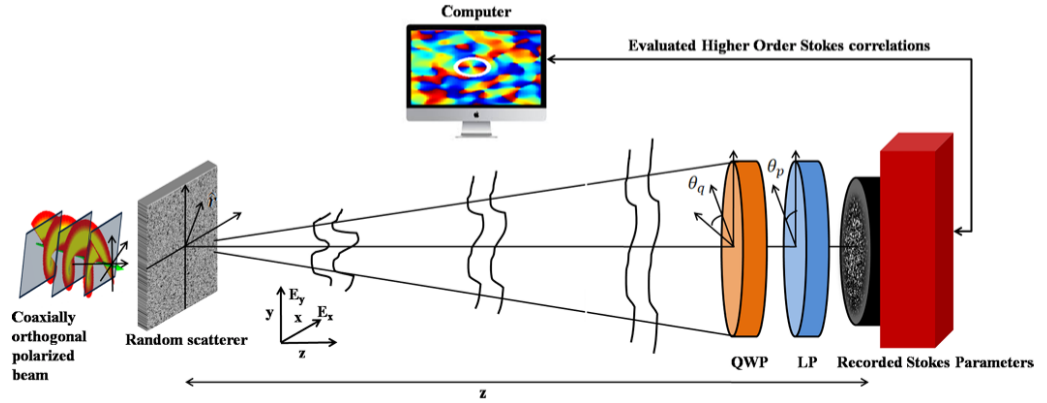
2.1 Introduction

FIGURE 2.1: Conceptual representation of the proposed technique studied in this report. Generation of random electromagnetic fields by orthogonally polarized light. x and y polarization components represent twisted and non-twisted wavefronts of the incident light. The CCD records intensity speckle patterns at the observation plane [Sarkar et al. (2021)].

A study [Sarkar et al. (2021)] is done to understand the method on the topological charge and the entire phase structure of a vortex beam disrupted by a random scattering medium may be determined quantitatively using a non-interferometric

approach. In this approach, a non-vortex beam with an orthogonal polarisation state co-axially enters the scattering medium with a vortex beam with an arbitrary topological charge. The complex polarisation correlation function and the twisted modes are obtained from the Stokes parameters of the random scattered field. The Stokes parameters' two-point correlations create a 4X4 matrix with a total of 16 components. Only four of the matrix's 16 components are employed to extract the real and imaginary sections of the complex polarisation correlation function, which are then used in the reconstruction of twisted wavefronts.

With a point of indeterminate phase in the nucleus, the vortex beam has a well-defined helical (twisted) phase structure. A phase factor $\exp(\iota * \phi * \ell)$ characterizes the twisted phase distribution of the vortex mode, where the azimuthal coordinate with respect to the beam axis and ℓ is an integer that represents the azimuthal mode index (topological charge) of the vortex beam. For both basic and practical reasons, the topological charge (TC) of the vortex beam is an important parameter determining the TC or OAM related to a beam becomes crucial as a result. The helical wavefront of the light must be evaluated in order to estimate the TC, and numerous methodologies have been presented for this purpose interference and diffraction are two of these strategies. These approaches, however, are mostly confined to the transmission of vortex beams across homogeneous material or empty space. The passage of the vortex beam through the scattering medium, on the other hand, produces a speckle pattern, which is a coherent random pattern. Remote sensing, imaging, and optical communication all rely on the propagation of such beams over random scattering surfaces. Due to the inhomogeneity of the optical path lengths of the scattering media, the coherent beam scrambles, resulting in laser speckles. As a result, measuring the incident vortex beam's topological charge and quantitative phase structure from the scrambled speckle pattern is a challenging process. The method studied here is to utilize a correlation of the Stokes parameters (SPS) of a randomly distributed field, to quantitatively measure the topological charge and phase structure of an incoming vortex beam.

2.2 Theoretical Analysis

As mentioned before in Chapter 1 [Sarkar et al. (2021)], Consider a monochromatic transversely polarised field with orthogonal axes x and y. One polarisation component has a twisted phase structure, while the other does not, and the two are coaxially propagating along the z-axis. The complex field at $z = 0$ in the transverse plane is written as

$$E(\hat{i}) = A_l(\hat{i}) * \exp(\iota * \ell * \phi)\hat{e_x} + A(\hat{i})\hat{e_y} \tag{2.1}$$

where r is the spatial location vector in the transverse plane and $\hat{e_x}$, and $\hat{e_y}$ are the horizontal and vertical polarisation states of the light, respectively. The amplitude of the vortex beam is $A_l(r)$, while the amplitude of the nonvortex beam is $A(r)$. The spiral phase structure of the vortex beam with the topological charge (ℓ) is represented by $\exp(\iota * \ell * \phi)$. The coherent beam now travels through a random scattering medium and arrives at an observation plane in any arbitrary plane z.

$$E(r) = FR(E(r) * \exp(\iota * \Delta(r))) \tag{2.2}$$

where $E(r)$ is the scattered field at the observation plane and $\Delta(r)$ is the spatial random phase. FR is the Fresnel transform corresponding to a distance z. Now the coherent beam propagates through a random scattering medium and reaches an observation plane located at any arbitrary plane z. The complex field in the observation plane is

$$E(r) = (\exp(\iota * k * z)/\iota * \lambda * z)(\exp(\iota * k * |r^2|/2 * z)) \int (E(\hat{r}) \exp(\iota * k * |\hat{r^2}|/2 * z)X$$
$$\exp(-\iota * k * (\hat{r} \cdot r)/z))d\hat{r} \tag{2.3}$$

where λ and $k = 2\pi/\lambda$ are the wavelength and wave number of the light, respectively. The Fresnel approximation is utilized by considering a large z value in comparison to these sources and the observation area of interest.

By considering a large z value in comparison to the source and the observation region of interest, the Fresnel approximation is used.

$$\therefore S_n(r) = E^*(r)\sigma^n E(r) \tag{2.4}$$

where $n = 0, 1, 2, 3$ and σ^n is a 2X2 identity matrix and three Pauli's spin matrices.

$$E(r) = \begin{bmatrix} E_x(r) \\ E_y(r) \end{bmatrix} \tag{2.5}$$

$$S_n(r) = \sum_{a,b} \sigma_{ab}^n (E_a^*(r))(E_b(r)) \tag{2.6}$$

where $a, b = x, y$

The SPs' variation around their average value is defined as

$$\delta S_n(r) = S_n(r) - \langle S_n(r) \rangle \tag{2.7}$$

where $n = 0, 1, 2, 3$ and $S_n(r)$ is the SP at a particular spatial point and $\langle S_n(r) \rangle$ represents its ensemble average.

Ensemble averaging is substituted by spatial averaging, assuming spatial stationarity and ergodicity in space at the observation plane and observing that $r_2 = r_1 + \Delta r_1$, ensemble averaging is replaced by spatial averaging. Now a 4 x 4 matrix $C_{nm}(\Delta r)$ is used to represent all possible pairings of two-point SP correlation

$$C_{mn} = \langle \nabla S_n(r_1) \nabla S_m(r_1 + \nabla r) \rangle \tag{2.8}$$

where $n, m = 0, 1, 2, 3$

Spatial averaging is used to derive elements of the correlation matrix for polarised light. The given equation, which contains 16 components, explains the relationships between the SP fluctuations. Calculations obtain 16 elements but the requirement is of only 4 to examine the complex polarization correlation function. From these 4 equations, real and imaginary parts of the complex polarization correlation function are obtained which helps in obtaining the function.

$$C_{Re}(\nabla r) = C_{20}(\nabla r) + C_{21}(\nabla r) \tag{2.9}$$

$$C_{Im}(\nabla r) = C_{30}(\nabla r) + C_{31}(\nabla r) \tag{2.10}$$

$$C(\nabla r) = C_{Re}(\nabla r) + \iota * C_{Im}(\nabla r) \tag{2.11}$$

where $C(\nabla r)$ is the complex polarization correlation function, it is the main result and is used to recover the vortex wavefront from randomly scattered light.

2.3 Experimental Analysis

Experimental Setup for recovery of topological charge from incident vortex beam as shown above. The setup is the same as given in [Sarkar et al. (2021)]. The spatially
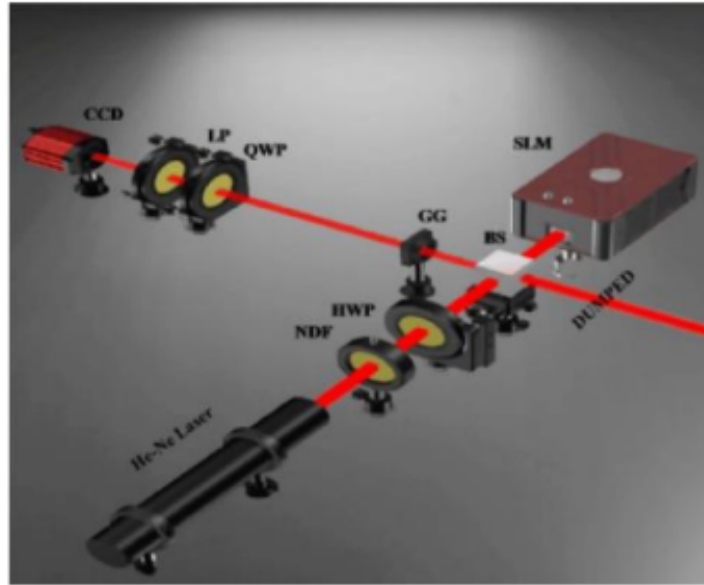

FIGURE 2.2: Experimental Setup [Sarkar et al. (2021)]

filtered collimated He-Ne laser light beam is attenuated with a neutral density filter and oriented at 45° with respect to the horizontal direction using a half-wave plate. The beam splitter divides the 45° polarised beam into two equal-intensity beams (BS). The structure of the vortex beam is shown on a phase-only SLM with a resolution of 1920 × 1080 and a pixel pitch of 8um that is illuminated by a beam transmitted from the BS. As a result, the vortex information's structure is fed into the x-polarization component of the beam, but the y-polarization component stays

unchanged, i.e., there is no vortex. The beam from the SLM reflects off the BS and goes into the ground glass, where random scattering distorts the incident light and produces a speckle pattern. Employment of optical elements to measure the SPS in order to identify the polarisation states of randomly scattered light. The random light is then filtered by a linear polarizer after passing through a quarter wave plate (QWP) that is rotated at an angle with respect to the x direction. The LP's transmission axis is aligned with the QWP in the x direction, and the resulting field is collected by a CCD camera. The CCD camera records the intensity of speckle patterns. Using the following equations, the four SPs are calculated from the recorded speckle patterns;

$$S_0(r) = I(0°, 0°) + I(90°, 90°) \tag{2.12}$$

$$S_1(r) = I(0°, 0°) - I(90°, 90°) \tag{2.13}$$

$$S_2(r) = I(45°, 45°) - I(135°, 135°) \tag{2.14}$$

$$S_3(r) = I(0°, 45°) - I(0°, 135°) \tag{2.15}$$

where $I(\theta_q, \theta_p)$ is the intensity at the observation plane. θ_q is the orientation of the optic axis of the quarter-wave plate with the axis of the polarizer and θ_p is the angle of the polarizer with the x-axis.

As described in the theoretical analysis section, the correlations of the fluctuations of the SPs are determined from empirically observed SPs.

2.4 Simulations

Simulations of the experimental setup are done to obtain the desired results of obtaining the topological charge and the twisted wavefront. An electric field is considered to have the x-component loaded with the twisted phase and the y-component taken to be a plane wave. A window of 1000 units and an aperture of 30 units are considered for plane wave and vortex components. The vortex component here is made in the form of a function with the input variable as I which is the topological charge, this is done for the purpose of efficiency. Now after the components of the
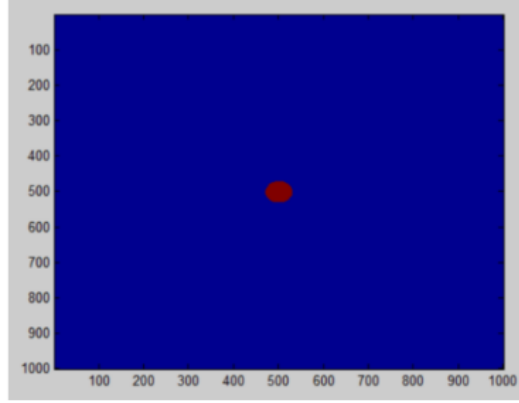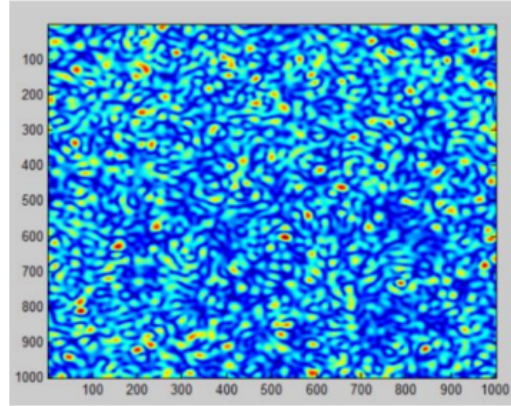
FIGURE 2.3: Window with aperture at center

FIGURE 2.4: Speckled Beam

complex electric field are obtained, they are passed through a randomly scattering medium, i.e., ground glass. Here the field components get randomly distorted and a random phase is introduced in the field.

As can be observed initially the ground glass is defined by providing it with pixel size, interval, etc., in the later part the formulation is done to obtain the random scattering pattern. Here ρ_m is the coherence length of ground glass. The term C_{a2} is responsible for generating scatter in the fields in the exponential term of C_{a2} the parameter n decides the amount of scattering to be done, a higher value of n means more scattering will occur and vice-versa. For simulation here n is taken to be 3. Now C_{d2} is element-wise multiplied by both the components of the electric field.

Here the vortex beam of topological charge $\ell = 1$ is being considered, but it can take any value of topological charge. The electric field components are then in E_1 and E_2 are Fourier transformed and then shifted to obtain a randomly scattered beam. As can be seen, the twisted wavefront has been lost due to scattering.

2.4.1   Stokes Parameters

Stokes Parameters are the four measurable quantities that can describe a state of polarized light. The first parameter describes the total intensity of the optical field. The remaining three parameters explain the different polarization states. It overcomes the problem of the optical amplitude. The Stokes Parameters are

$$S_0 = E_x * E_x^* + E_y * E_y^* \tag{2.16}$$

$$S_1 = E_x * E_x^* - E_y * E_y^* \tag{2.17}$$

$$S_2 = E_x * E_y^* + E_y * E_x^* \tag{2.18}$$

$$S_3 = \iota * (E_x * E_y^* + E_y * E_x^*) \tag{2.19}$$

For simulation purposes amplitude of the optical beam has been used to find the Stokes parameter and for experimental purposes, the intensity is used. Here we describe the total intensity, S_1 describes the linear vertical or horizontal polarization, S_2 describes the linear $45°$ or $-45°$ polarization and S_3 describes the amount of right or left circular polarization. By measuring the generalized Stokes parameter, the topological charge and helical phase structure of the coherent vortex beam may be recovered from the speckle pattern. As discussed earlier the correlation of the fluctuation of SPs of the speckled beam provides a 4×4 correlation matrix C_{mn} with a total of 16 elements. The cross-covariance of the measured SPs is digitally evaluated by taking spatial averaging and spatial ergodicity. This is accomplished by converting a piece of the detected SP into a matrix $S_n^\alpha(x, y)$, which represents one random field SP realization. The pixel spatial coordinates x and y can be any value between 300×300. $\sum_\alpha [\Delta S_m^\alpha(x, y) \Delta S_n^\alpha(0, 0)]/M$ is the cross-covariance of the SPs for different realizations of the random patterns. Here M is the different number of realizations of $S_n^\alpha(x, y)$ occurring due to the pixel-by-pixel movement of $S_n^\alpha(x, y)$ over

the measured SP. A random pattern with a size of 1000×1000 pixels is considered. Scanning $S_n^\alpha(x, y)$ through the random pattern in two dimensions yields 700 x 700 distinct realizations for averaging.

Therefore, inside the correlation function, the four elements of the correlation function matrix are found using the Stokes parameters' cross-covariance. The real and imaginary parts of the complex polarization function are obtained which is used in finding the complex polarization correlation function.

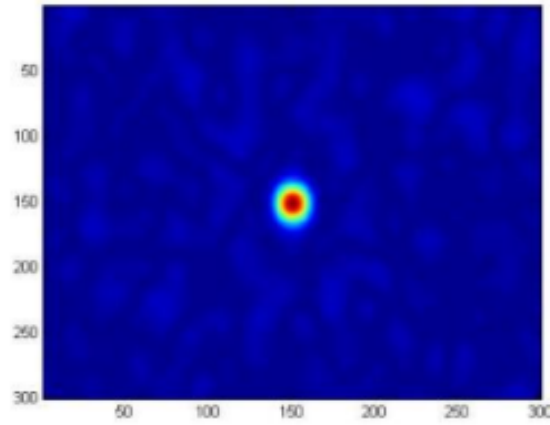## 2.5   Results and Discussions

FIGURE 2.5: Amplitude Distribution of the Complex Polarization Correlation Function for $\ell = 1$

The Simulation results of the phase and amplitude distribution of complex correlation function $C(\Delta r)$ are obtained for three different topological charge or OAM modes. Figures 2.5, 2.6, and 2.7 represent the amplitude distribution for topological charges $\ell = 1, 2, 3$ in simulated results. As it can be seen the Vortex structure and phase of the vortex beam have been recovered from the speckled beam through the method of Stokes Parameter correlation. Although the phase and amplitude of the vortex beam are recovered it still contains some distortion which infers to the loss of some information. This distortion in the output result can be blamed on the plane wave component of the input complex electric field. The plane wave causes
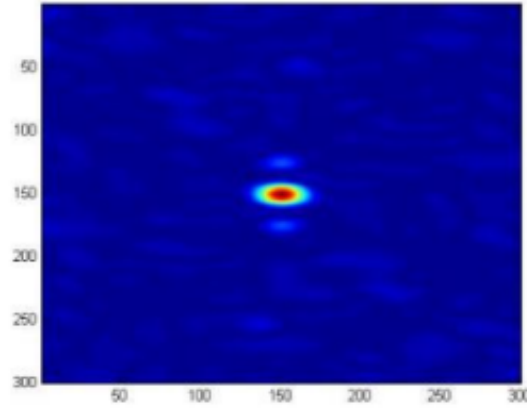
FIGURE 2.6: Amplitude Distribution of the Complex Polarization Correlation Function for $\ell = 2$
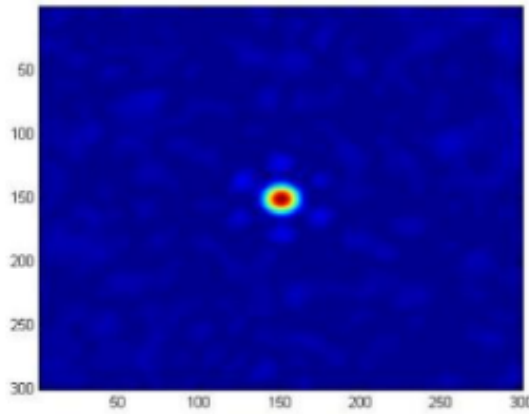

FIGURE 2.7: Amplitude Distribution of the Complex Polarization Correlation Function for $\ell = 3$

the background noise. The intensity profile shows that the radius of the "doughnut" shaped intensity profile increases with an increase in topological charge. A large topological charge has an impact on the reconstruction quality of the coherent vortex beam. One of the identified reasons for this is that when the vortex beam of higher topological charge is propagating through the ground glass it experiences more random scattering making the reconstruction through correlation difficult.

Chapter 3

Conclusion and Perspectives

3.1 Conclusions

A vortex beam is a light wave with no intensity due to a singularity in phase at the nucleus of its wavefront structure [Shen et al. (2019)]. The vortex beam has a well-defined helical (twisted) phase structure in the nucleus, with an indeterminate phase point. The photons' helical wavefronts carry an orbital angular momentum (OAM) of $\ell * h$ per photon in the vortex beam, and each OAM mode is identifiable by the number of twists in the helical wavefronts. The OAM beam has a lot of potential in terms of practical applications. Particle entrapment, free-space optical communication, and other applications are examples. On the other hand, the OAM has been used to build an infinite-dimensional discrete basis in optical quantum communication to boost the encoded information's transmission capability.

The method studied here is from a correlation of the Stokes parameters (SPs) of a randomly distributed field, quantifying the topological charge and phase structure of an incoming vortex beam [Sarkar et al. (2021)]. This method is used for the determination of the topological charges of the vortex beam from the laser speckle. The simulation work is done to verify the Stokes parameter correlation and to successfully obtain the twisted wave structure and phase profile of a vortex beam. This method is then extended to determine the wave because of the non-interferometric method, the technique is robust and does not require a separate reference beam. The

technique also has some limitations which require further work. One of the main limitations of this technique is that it does not work for the case of multiple topological charge beams and the intensity and phase profile recovered still contain distortion to some extent. This can be overcome by performing the deconvolution of the Complex polarization correlation function, which will remove the plane wave component from that of the vortex component, this plane wave component is responsible for the distortion in the results. This technique is significant in imaging polarization-sensitive objects across random media, optical communication, and characterizing random electromagnetic beams.

3.2   Future Scope

The results when a lower intensity factor (IF) is used are less qualitative than the ones with a higher intensity factor. However, the intensity factor value has implications for the computational cost. So, if the IF is higher the computational cost and the entire process of obtaining the results becomes expensive. So, I tried to design a denoising model i.e., a convolutional denoising autoencoder in order to improve the results from a lower IF to a higher IF. Therefore, using Machine Learning we can try and improve the results with lower computational cost if we have adequate data to train the model.

Appendix A

MATLAB Code

In this section, we cover the MATLAB code used for generating the window with an aperture at the center, a speckled beam, and amplitude distribution of complex polarization correlation function for various values of ℓ.

```matlab
p=zeros (1000);
for x=1:1000,
    for y=1:1000,
        if (x-501) ^2 + (y-501)^2 <= (30)^2,
        p(x,y) = 1;
    end
end
end
```

LISTING A.1: Generation of Plane Wave

```matlab
p1=zeros (1000);
for x=1:1000,
    for y=1:1000,
        phi = atan2((y-501), (x-501));
        if (x-501) ^2 + (y-501) ^2 <= (30)^2,
            p1(x,y) = exp(1i*1*phi);
    end
end
end
```

LISTING A.2: Generation of Vortex Wave

```matlab
dx =1; %% in mm, SLM pixel
dy=dx;
lx=999; %% mm
ly=lx;
[m,n]=meshgrid(-0.5*lx:dx:0.5*lx,+0.5*ly:-dy:-0.5*ly);
[wmax, smax] =size(m);
```

LISTING A.3: Creating Mash Grid

```matlab
Rho_m=0.040;
A_g2=exp (-(m.^2+n.^2)/Rho_m^2);
C_a2=(fft2(rand(wmax,smax)-0.5));
H2=(fft2(A_g2));
C_d2= (ifft2(C_a2. *real(H2)));
C2=exp(1i*20*pi*(real(C_d2))/max(real(C_d2(:))));
C2=C2(1:1000,1:1000);
H1=fftshift(fft2(p.*C2));
H2=fftshift(fft2(p1. *C2));
```

LISTING A.4: Generation of Scatter

```matlab
Ex=H1. /max(abs(H1(:)));
Ey=H2. /max(abs(H2(:)));
I_0=(Ex+Ey). *conj(Ex+Ey);
I_1=I_0(1:1000,1:1000);
I_d=0;
I_av=0;

l_u=0;
for n_r=-350:350,
    l_u=l_u+1;
    l_v=0;
    for m_r=-350:350,
        l_v=l_v+1;
        Ir_n1=I_1(501+n_r,501+m_r);
```

```matlab
15          I_av=I_av+Ir_n1;
16          clear Ir_n1 Ir_n1;
17      end
18  end
19
20  l_u=0;
21  for n_r=-350:350,
22      l_u=l_u+1;
23      l_v=0;
24      for m_r=-350:350,
25          l_v=l_v+1;
26          I_r1=I_1(351+n_r:650+n_r,351+m_r:650+m_r);
27          I_r2=I_1(501+n_r,501+m_r);
28          I_cor=(I_r1-(I_av/200^2)).*(I_r2-(I_av/200^2));
29          I_d=I_d+I_cor;
30      end
31  end
32  clear I_r1 I_r2 I_cor Ir_n1 Ir_n2;
33  I_1=I_d./(I_av)^2;
```

LISTING A.5: Amplitude Distribution and Stokes Parameter generation

Bibliography

Chen, M. L., Jiang, L., and Sha, W. (2018). Orbital angular momentum generation and detection by geometric-phase based metasurfaces. *Applied Sciences*, 8:362.

Forbes, A. (2017). Controlling light's helicity at the source: Orbital angular momentum states from lasers. *Philosophical Transactions of The Royal Society A Mathematical Physical and Engineering Sciences*, 375:20150436.

Jia, P., Yang, Y., Min, C., Fang, H., and Yuan, X.-C. (2013). Sidelobe-modulated optical vortices for free-space communication. *Optics letters*, 38:588–90.

Kozawa, Y., Matsunaga, D., and Sato, S. (2018). Superresolution imaging via superoscillation focusing of a radially polarized beam. *Optica*, 5:86.

Omatsu, T., Miyamoto, K., and Lee, A. J. (2017). Wavelength-versatile optical vortex lasers. *Journal of Optics*, 19(12):123002.

Padgett, M. (2017). Orbital angular momentum 25 years on. *Optics Express*, 25:11265.

Sarkar, T., Parvin, R., Brundavanam, M. M., and Singh, R. K. (2021). Higher-order stokes-parameter correlation to restore the twisted wave front propagating through a scattering medium. *Phys. Rev. A*, 104:013525.

Shen, Y., Wang, X., Xie, Z., Min, C., Fu, X., Liu, Q., Gong, M., and Yuan, X. (2019). Optical vortices 30 years on: Oam manipulation from topological charge to multiple singularities. *Light, Science & Applications*, 8.

Takeda, M., Wang, W., Duan, Z., and Miyamoto, Y. (2005). Coherence holography. *Opt. Express*, 13(23):9629–9635.

Takeda, M., Wang, W., Naik, D., and Singh, R. k. (2014). Spatial statistical optics and spatial correlation holography: A review. *Optical Review*, 21:849.

Wang, J. (2016). Advances in communications using optical vortices. *Photonics Research*, 4:B14–B28.

Wang, X., Nie, Z., Liang, Y., Wang, J., Li, T., and Jia, B. (2018). Recent advances on optical vortex generation. *Nanophotonics*, 7.

Yao, A. and Padgett, M. (2011). Orbital angular momentum: Origins, behavior and applications. *Advances in Optics and Photonics*, 3:161–204.

Zhang, L., Shen, B., Zhang, X., Huang, S., Shi, Y., Liu, C., Wang, W., Xu, J., Pei, Z., and Xu, Z. (2016). Deflection of a reflected intense vortex laser beam. *Phys. Rev. Lett.*, 117:113904.

Zhu, L. and Wang, J. (2019). A review of multiple optical vortices generation: methods and applications. *Frontiers of Optoelectronics*, 12.

Sarkar et al. (2021) Takeda et al. (2005) Shen et al. (2019) Omatsu et al. (2017) Zhang et al. (2016) Takeda et al. (2014) Forbes (2017) Wang et al. (2018) Zhu and Wang (2019) Padgett (2017) Yao and Padgett (2011) Chen et al. (2018) Kozawa et al. (2018) Wang (2016) Jia et al. (2013)